Manuscript

A comparative study of earthquake source models in high-order accurate tsunami simulations

Mahya Hajihassanpour[a,b], Boris Bonev[a,1*], Jan S. Hesthaven[a]

[a]École polytechnique fédérale de Lausanne (EPFL), CH-1015 Lausanne, Switzerland
[b]Sharif University of Technology, Tehran, Iran

Abstract

The discontinuous Galerkin method is used to solve the non-linear spherical shallow water equations with Coriolis force. The numerical method is well-balanced and takes wetting/drying into account. The two fold goal of this work is a comparative study of dynamic and static tsunami generation by seabed displacement and the careful validation of these source models. The numerical results show that the impact of the choice of seabed displacement model can be significant and that using a static approach may result in inaccurate results. For the validation of the studies, we consider measurements from satellites and buoy networks for the 2011 Tohoku event and the 2004 Sumatra-Andaman tsunami. The results confirm that the method is appropriate for large-scale tsunami simulations and early warning systems.

Keywords: Static and dynamic seabed displacement, Tsunami modeling, Shallow water equations, Well-balanced scheme, Wetting and drying, Discontinuous Galerkin method

1. Introduction

Tsunamis are oceanic gravity waves generated by large sea level surface displacements. Such displacements can be generated by volcanic eruptions (Ulvrova et al., 2016), landslides (de la Asunción et al., 2016), asteroid impacts (Ezzedine et al., 2015) or earthquakes (Bonev et al., 2018). Tsunamis generated by earthquakes are commonplace and can cause considerable damage to human lives and infrastructures. There are various mathematical models, which can be used to model and predict the dynamics of tsunami waves. Such mathematical models should be able to accurately predict the sea surface displacement, velocity and arrival times of waves reaching the coastline. The resulting inundation area and the overall computational cost can also be of interest. The models can be broadly classified as follows:

- 3D models: The governing equations are derived without integrating over the depth. These are non-hydrostatic models, for instance the Navier-Stokes or Euler equations. Although these are accurate models, their computational cost is substantial and currently not applicable to large scale predictive problems (Mori et al., 2015; Oishi et al., 2013; Saito and Furumura, 2009).
- 2D models: These models are derived by integrating over the depth and can be either non-hydrostatic (Boussinesq-type equations) (Baba et al., 2017; Baba et al., 2015) or hydrostatic (shallow water equations) (Brecht et al., 2018; Rannabauer et al., 2018).

Typically, the 3D models are more accurate than the 2D models such as the shallow water equations, but their computational cost make them impractical for the purpose of tsunami predictions. The computational cost and accuracy of the tsunami simulations not only depend on the mathematical model but also on the numerical method being applied. In the context of tsunami simulations various methods have been applied. Among them are the finite difference (FD) (Flouri et al., 2013; Wang and Liu, 2007), finite volume (FV) (Clain et al., 2016; LeVeque et al., 2011), Finite element (FE) (Takase et al., 2016), discontinuous Galerkin (DG) (Blaise and St-Cyr, 2012; Blaise et al., 2013; Bonev et al., 2018; Castro et al., 2016; Seny et al., 2014) and hybrid (Asai et al., 2016; Olabarrieta et al., 2011) methods. While all of these methods have their strengths and weaknesses, the discontinuous Galerkin method stands out in the context of wave problems as it offers high accuracy and efficiency through h/p adaptivity and parallelity.

The effects of the earthquake and the subsequent seabed displacement enter the shallow water equations as a

---

source term. This source term can be time-independent (the passive/static approach) (Ortega et al., 2011; Reckinger et al., 2014; Suppasri et al., 2010; Yamazaki et al., 2011b) or time-dependent (the active/dynamic approach) (Dutykh and Dias, 2009; Dutykh et al., 2013; Ohmachi et al., 2001; Ohta et al., 2012; Suppasri et al., 2010; Uphoff et al.; Vogl and LeVeque, 2017; Yamazaki et al., 2011a). In the static approach, only the final deformation of the seabed is considered. This displacement is introduced into the simulation by displacing the initial sea surface according to the deformation of the seabed. Several assumptions are made in this static approach. First of all, the wavelengths of the tsunami waves are assumed to be much larger than the depth of the ocean. The vertical acceleration of the water is neglected as it is small in comparison to the gravitational acceleration on the water mass that is lifted, which causes a uniform velocity profile in the horizontal direction. Secondly, the vertical seabed displacement is assumed to be instantaneous. This is accurate if the timescale of the earthquake rupture is much smaller than the timescale of the tsunami propagation. Lastly, the horizontal displacement of the seabed is usually neglected, unless the horizontal displacement is large relative to the vertical displacement. The static approach can consist of a single fault (Ortega et al., 2011; Reckinger et al., 2014) or multiple faults (Suppasri et al., 2010; Yamazaki et al., 2011b). The multi-fault case can be used to increase the resolution of the seabed displacement due to an underwater earthquake relative to the single-fault. In contrast to the static approach, in the dynamic approach, the full transient motion of the seabed displacement due to an underwater earthquake is considered. The transient seabed displacement can be obtained by considering a simple time function for temporal changes (Dutykh and Dias, 2009; Dutykh et al., 2013; Ohmachi et al., 2001; Suppasri et al., 2010; Yamazaki et al., 2011a), recovering an initial condition from buoy data (Blaise et al., 2013), a quasi real-time fault model (Ohta et al., 2012) or solving the equations of elasticity (Uphoff et al.; Vogl and LeVeque, 2017). Similar to the static approach, the dynamic approach can be modeled as single-fault (Dutykh and Dias, 2009) or multi-fault (Dutykh et al., 2013; Ohmachi et al., 2001; Suppasri et al., 2010; Yamazaki et al., 2011a).

In this work, we consider the depth-averaged shallow water equations in Cartesian coordinates with Coriolis force. We employ the numerical algorithm presented in (Bonev et al., 2018), which employs curved elements and dynamic mesh refinement. Moreover, a wetting/drying treatment, which is also presented in (Bonev et al., 2018) handles dry areas such as continental land masses. Simulations of the 2011 Tohoku and 2004 Sumatra-Andaman tsunamis are considered using both dynamic and static seabad deformation models. We wish to investigate the effect of the dynamic seabed displacement model on the accuracy of the numerical restuls. We asesss the accuracy of the computed results and the respective source models with the help of real-world data, which is readily available for both tsunamis.

The paper is organized as follows: In Section 2, we discuss the source models that model the generation of tsunamis through an underwater earthquake. This includes the discussion of static and dynamic seabed displacement approaches. In Section 3 we investigate the impact of the static and dynamic approaches on the numerical results. To this end, the 2011 Tohoku and 2004 Sumatra-Andaman tsunamis are investigated. We compare results to measurements to assess their accuracy. We state our conclusion in Section 4. In Appendix A, we discuss the governing equations. Appendix B gives an overview of the numerical method (Bonev et al., 2018), comprising the spatial discretization and the time integration. Finally, the wetting/drying method, as well as the well-balanced and positivity preserving properties are given in Appendix C.

2. Tsunami generation

For the static seabed displacement approach we assume that fault parameters such as the longitude (Lon), latitude (Lat), depth, length, width, strike, dip, rake and slip are known. Using these parameters, the Okada solution can be computed (Okada, 1985), to recover the seabed displacement caused by the earthquake thrust. For a dynamic approach, two additional parameters, i.e., the rupture velocity (or the rupture initiation time) and rise times are needed. There is an explicit relation between the rupture velocity and the rupture initiation time. If the rupture velocity is considered to be constant in each subfault i, then

$$t_0^{i+1} = \frac{l^i}{V^i} + t_0^i, \quad i = 1, 2, \dots, N_f \tag{1}$$

where l^i, V^i, t_0^i are the length, rupture velocity, rupture initiation time of the i-th subfault and N_f the total number of subfaults. Here we assume that $t_0^1 = 0$.

If a fault has been divided into N_f subfaults, then the total displacement of the seabed at position $\boldsymbol{r} = \{x, y, z\}^T$ can be considered as the sum of displacements for each subfault, i.e.,

$$\delta(\boldsymbol{r}) = \sum_{i=1}^{N} O^i\left(\boldsymbol{r}^i, l^i, w^i, d^i, \dots\right) \tag{2}$$

where O^i is the Okada solution in the i-th subfault. Note that the Okada solution computes a static seabed displacement. Thus, to achieve a dynamic rupture model, a time-activation function f^i is considered for each

subfault. In other words (2) is modified as

$$\delta(\boldsymbol{r},t) = \sum_{i=1}^{N} f^i(t,t_0^i,t_0^{i+1})\, O^i(\boldsymbol{r}^i,l^i,w^i,d^i,\dots), \tag{3}$$

where different activation functions $f^i(t,t_0^i,t_0^{i+1})$ can be used (Dutykh et al., 2013; Kundu, 2007; Yamazaki et al., 2011a). Here, a linear activation function (Yamazaki et al., 2011a) is used:

$$f^i(t,t_0^i,t_0^{i+1}) = \begin{cases} 0 & \text{if } t < t_0^i \\ \dfrac{t - t_0^i}{t_0^{i+1} - t_0^i} & \text{if } t_0^i \le t \le t_0^{i+1} \\ 1 & \text{if } t_0^{i+1} < t \end{cases}. \tag{4}$$

3. Numerical Results

In the following, we present numerical results with the implementation of the discontinuous Galerkin method (DGM) for the spherical shallow water equations. To understand the effects of the static and dynamic seabed displacement approaches on the tsunami waves, we compare the two models using two different tsunami events. These two tsunamis are the 2011 Tohoku and the 2004 Sumatra-Andaman events. The numerical results obtained for these two tsunamis are compared with the available measured data to assess their quality and the performance of the static and dynamic seabed displacement models. These two tsunamis are chosen as they are the two largest and most devastating events in recent decades, with plenty of data available. Moreover, their character is quite different as the earthquake that caused them have vastly differing fault dimension and rupture speeds.

3.1. Tohoku event

On March 11th, 2011, at 2:46 pm JST (05:46 UTC) a massive earthquake of magnitude $M_w = 9.0$ struck near the northeastern coast of Japan, resulting in massive seafloor displacement and high tsunami waves. The first significant waves reached Japan only 10 min after the earthquake struck, thus leaving very little warning time. This tsunami caused thousands of fatalities and financial damage of hundreds of billion dollars. The characteristics of this tsunami make it an interesting test case for our purposes.
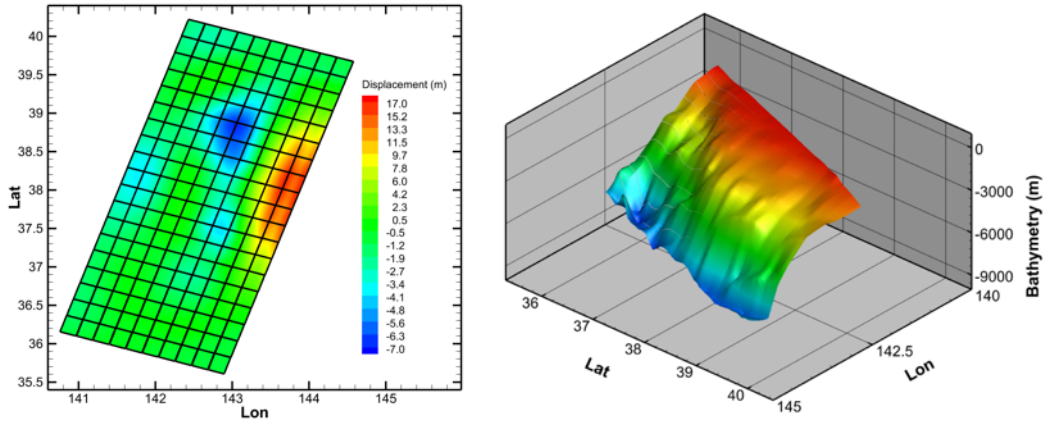

Figure 1: Left: subfaults and the seabed displacement for the Tohoku earthquake and Right: bathymetry in the corresponding subfaults.

To obtain the seabed displacement using the Okada model (Okada, 1985), subfault parameters are taken from the University of California, Santa Barbara (UCSB) database for big earthquakes (Shao et al., 2011). We use the parameters of model III presented in (Shao et al., 2011). These parameters include both static and dynamic parameters. In the aforementioned data, the number of subfaults in the strike direction is 19 and in down-dip direction 10, which results in the total number of $N_f = 190$ subfaults. The length of each subfault in the strike direction is 25 km whereas it is 20 km in the down-dip direction. The fault is situated between 35.74° and 40.09° northern latitude and between 140.91° and 144.42° eastern longitude. By inserting the fault parameters into (2), the final displacement of the seabed, which is shown in Fig. 1, is obtained. As shown in this figure, the maximum lift of the seabed is located on the eastern side of the fault. The bathymetry within the subfaults is illustrated in Fig. 1. Apart from the initial displacement, an accurate simulation requires accurate bathymetry data. Note that if the earthquake makes the topography shallower or deeper, both the near-field and the far-field solutions can be affected, as this would change the wave speed in the vicinity. Here, the maximum lift of the seabed is in an area

where the water is relatively deep, so the ratio between the maximum lift and the water depth is small. The dynamic rupture can be modeled by (3). The maximum displacement is about 17m upward and 7m downward. The dynamic rupture is rather short and almost static after 105 seconds.

The mesh generated for the Tohoku tsunami event is shown in Fig. 2. The initial mesh is an unrefined icosahedral mesh. We define an area of interest, which is selected for local refinement of the grid. This area is defined by the circle centered at -177° longitude, 12° latitude with a radius of 55°. The center and radius of the circle, as well as the level of refinement are selected to provide an appropriate mesh wide enough to capture waves traveling up to 12 hours from the origin of the tsunami. The grid in this area is refined locally five times, which yields the desired resolution in the area of interest, displayed in Fig. 2. It contains 14235 elements, of which most are located in the Pacific Ocean. As shown in Fig. 2, the mesh is considerably coarser on the opposite side of the sphere, which reduces computational cost. Using this approach, regions of interest can be defined and grids that are adapted to this region are generated automatically. We restrict ourselves to balanced non-conforming grids, in which only one hanging node is permitted at each interface. A balanced grid is characterized by the property that the difference in refinement levels of two neighboring elements cannot be greater than one. In other words, there are no more than three elements interfacing at one edge.
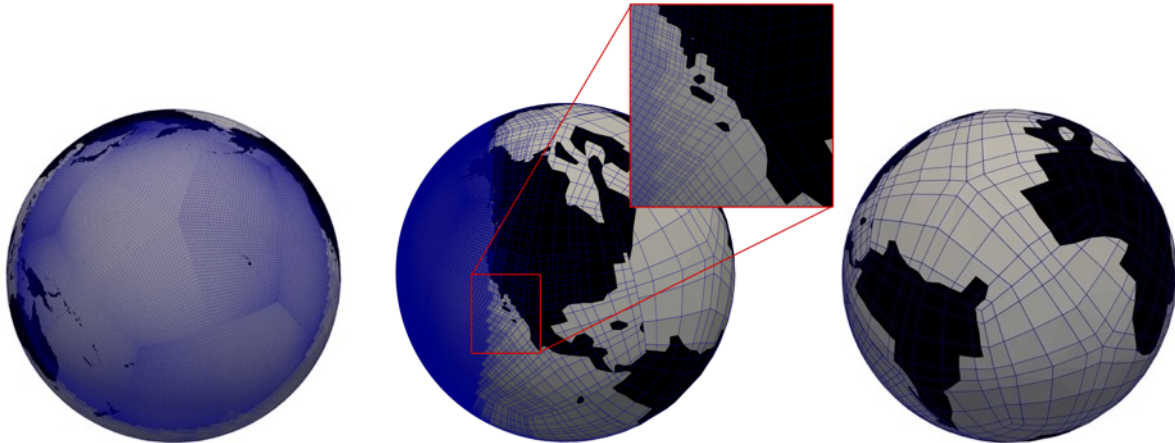

Figure 2: Mesh generated for the simulation of the Tohoku tsunami. We provide a more detailed discussion of the mesh generation in the text.

The propagation of the tsunami waves is shown at different times in the left column of Fig. 3. In this figure, we show the results obtained with the static seabed displacement approach and biquartic polynomials $N = 4$. As is clear, at initial time, the seabed displacement has been transferred to the water height. After a while, tsunami waves propagate into the Pacific Ocean and their amplitudes diminish.

The difference in sea surface height between the static and dynamic approach is also shown in Fig. 3. In this figure, numerical results obtained with the static approach are denoted by h_s and for the dynamic approach are denoted by h_d. In the middle column of the figure, contour levels ranging from -0.1m to 0.1m are shown, while in the right column contour levels between -1m and 1m are shown. Results presented in the right column show that differences between the two seabed displacement models are small when only large wave amplitudes are considered. It is clear that big waves affect the near field, which only makes up a small portion of the Pacific Ocean. Initially, the differences between the two approaches are large as expected. After 2 hours, however, we can see that differences are small. If we consider small amplitudes however, then the differences between results remain significant even in the far-field. This can be seen in the middle column. Therefore, an important factor in choosing the seabed displacement approach is whether the result needs to be accurate and where the zone of interest lies with respect to the tsunami source. If the zone of interest is located near the earthquake zone or if high accuracy is needed then the dynamic approach should be considered.

The comparison presented in Fig. 3 is qualitative as it only compares the results of the two models. Therefore it is valuable to present quantitative results. To do this, results obtained by the DG method are compared with buoy data. This buoy is the DART buoy 21418. The buoy data is collected by the DART tsunami monitoring network and are provided online by the National Data Buoy Center (NDBC) of the National Oceanic and Atmospheric Administration (NOAA) (Milburn et al., 1996). By subtracting the time-average from the buoy data, we eliminate the effect of tides, which are not considered in our model.
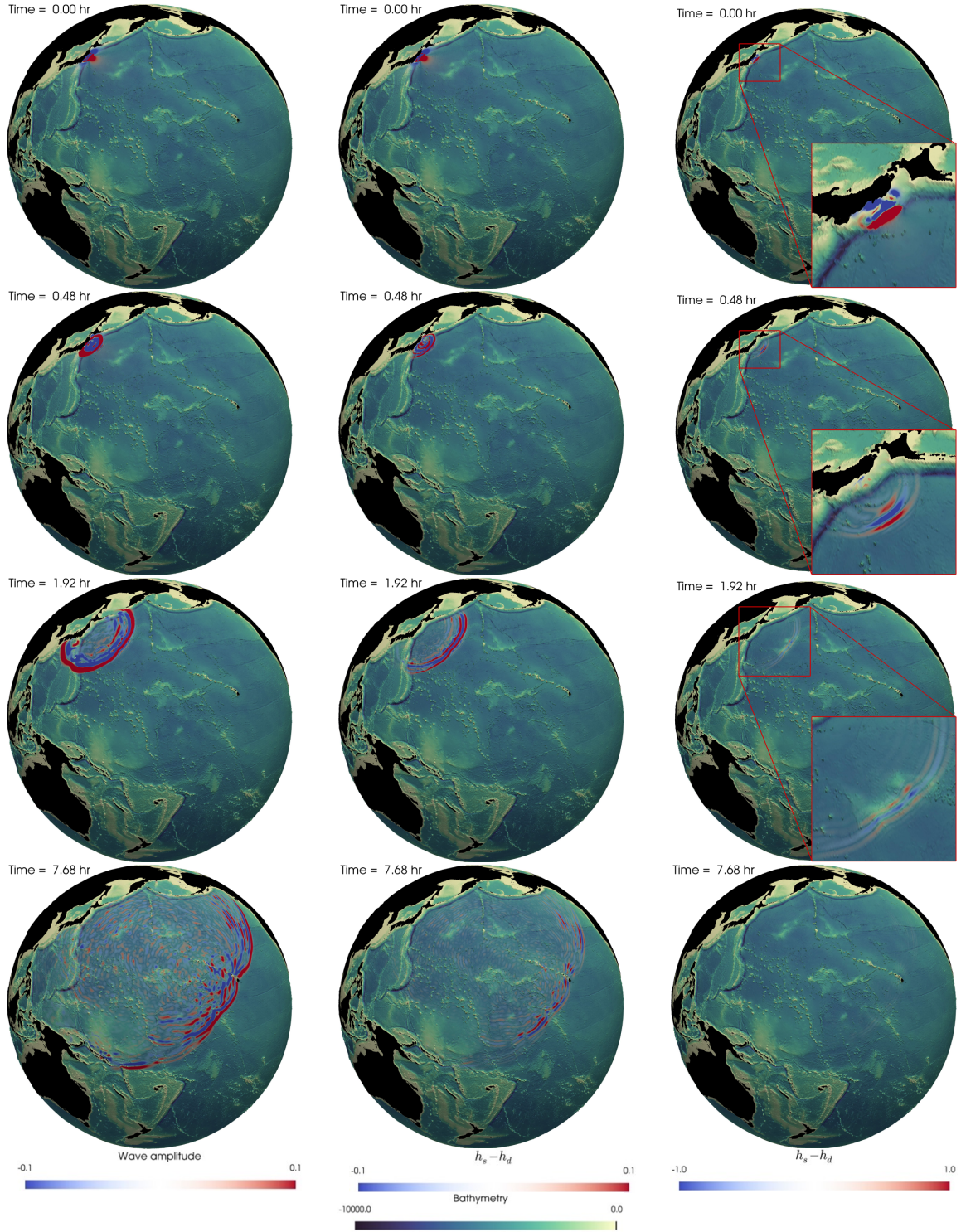
Figure 3: Propagation of tsunami waves and differences in wave amplitude between static and dynamic seabed deformations for the Tohoku tsunami. The left column indicates the propagation of tsunami waves, the middle column highlights small differences between -0.1m and 0.1m and the right column highlights large differences between -1m and 1m.

Here, we have performed numerical simulations using two polynomial degrees, $N = 2$ and $N = 4$ to understand effects of the polynomial degree on the numerical results. It is expected that using higher degree polynomials results in higher accuracy. For the buoy 21418, effects of the polynomial degree are shown in Fig. 4. As shown in this figure, using biquartic polynomials results in a higher accuracy compared to the results obtained with biquadratic polynomials. It is also clear that the biquartic polynomials capture the maximum water height more accurately than the biquadratic polynomials. This is expected as higher order methods are less dissipative and therefore better suited for large scale solutions where the solution is smooth in large parts of the domain. We

observe from this figure that the arrival time is correctly computed and the agreement with the buoy data is satisfactory. For both the static and dynamic seabed displacement approaches, using $N = 4$ results in more accurate results than $N = 2$.

The comparison of the static and dynamic seabed displacement approaches is presented in Fig. 5. The differences are not significant and there is only a slight advantage of the dynamic seabed displacement approach, which leads to better agreement in the buoy data. We observe that the predicted arrival time is in better agreement with the buoy data if the dynamic seabed displacement approach is used. The L_2-norm error calculated based on the differences between the numerical results using the static seabed displacement approach and the buoy data is 0.1357 while for the dynamic one is 0.1198. Therefore, we observe that the dynamic model performs slightly better than the static model.
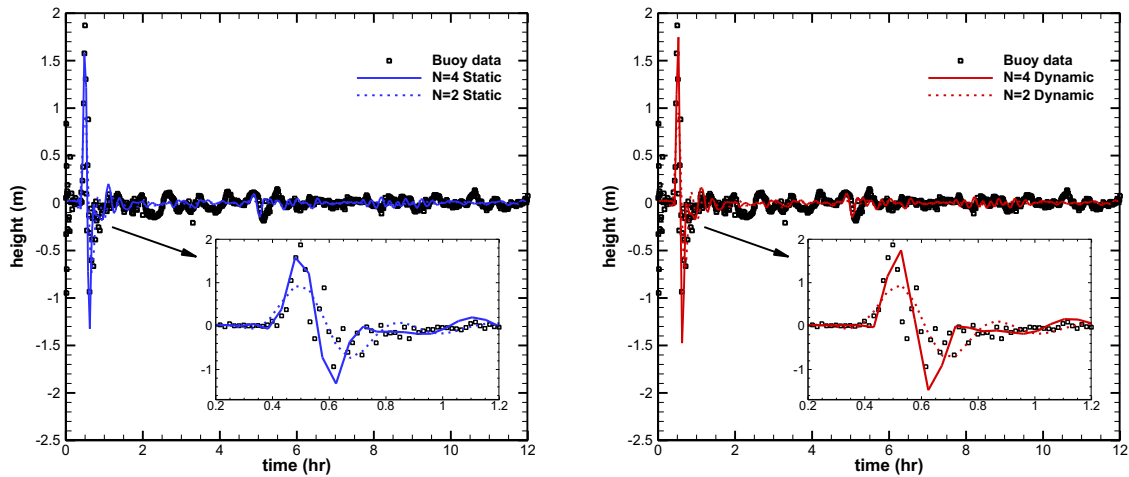

Figure 4: Effect of the polynomial degree on the computed sea surface height in comparison to the DART 21418 buoy measurements. Left: sea surface heights computed with static seabed deformation. Right: sea surface heights computed with dynamic seabed deformation.
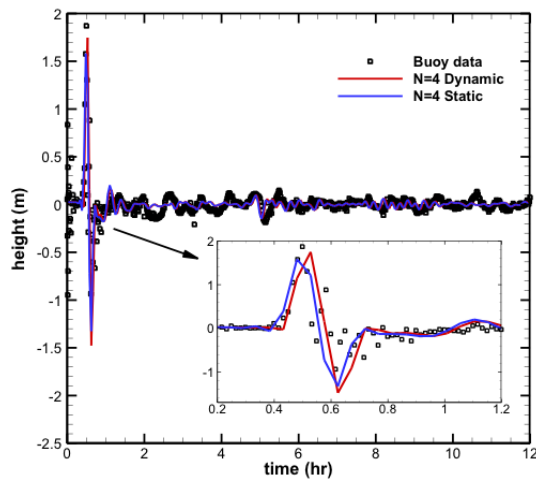

Figure 5: Comparison of the static and dynamic seabed deformation approaches using buoy data DART 21418.
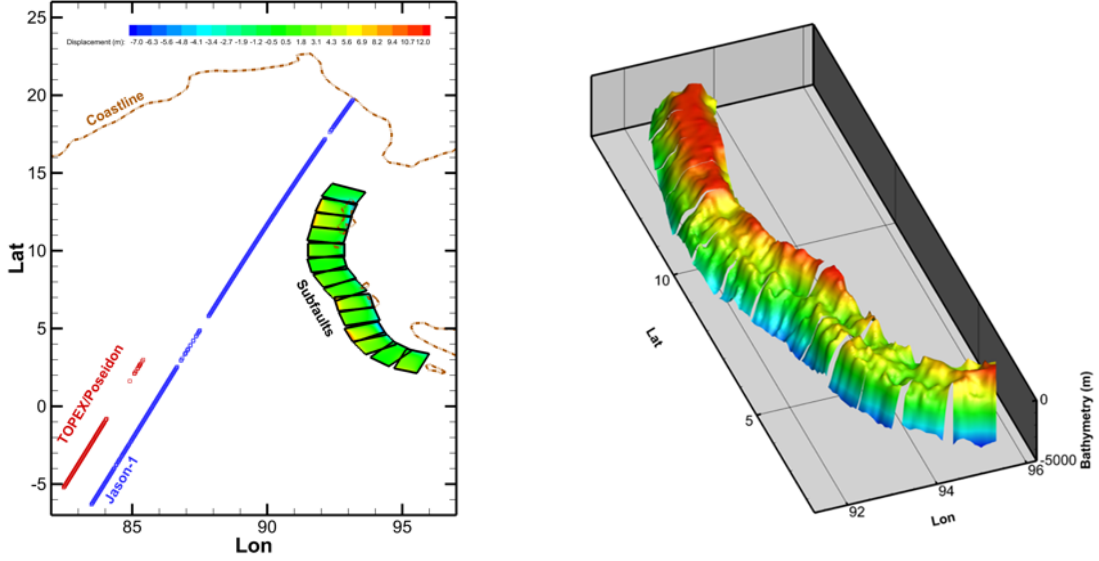
Figure 6: Left: Subfaults and seabed displacement of the Sumatra-Andaman earthquake. Satellite measurements from TOPEX/Poseidon are indicated in the figure. Right: Bathymetry in the corresponding subfaults.

3.2. Sumatra-Andaman event

On December 26th, 2004, at 0:59 AM UTC an earthquake of magnitude $M_w = 9.1 - 9.3$ struck near the west coast of Sumatra, Indonesia, resulting in tsunami waves which affected many surrounding nations. It is the third-largest earthquake ever recorded on a seismograph and has the longest ever recorded fault duration of about 10 minutes. This tsunami caused hundreds of thousands of fatalities and financial damage of hundreds of billion dollars. Its large fault size and the long fault duration as well as its destructive power make it an appropriate, yet challenging test scenario to compare the static and dynamic seabed displacement models.

Table 1: Earthquake parameters used for the simulation of the Sumatra-Andaman tsunami. Subfaults are ordered according to latitude.

subfaults	Lon	Lat	Depth	Length	Width	Strike	Dip	Rake	Slip	Initiation time	Rise time
1	95.54	2.13	10	100	150	290	10	71	16.5	0	48.5
2	94.5	2.57	10	100	150	310	10	91	0	31.96	48.5
3	93.64	3.33	10	100	150	330	10	104	14.9	136.85	37.5
4	93.16	4.15	10	100	150	340	10	105	29.1	167.62	117.3
5	92.88	5.18	10	100	150	345	10	102	10.4	227.09	138.7
6	92.63	6.12	10	100	150	350	10	100	23.4	254.98	62.1
7	92.53	6.78	10	100	150	330	10	90	9.4	282.41	38.5
8	92.08	7.64	10	100	150	335	10	86	11.5	308.57	111.2
9	91.64	8.6	10	100	150	350	10	99	1.5	334.06	63.9
10	91.51	9.6	10	100	150	0	10	106	12	396.16	51.3
11	91.48	10.66	10	100	150	10	10	115	6.1	433.33	79
12	91.63	11.56	10	100	150	10	10	115	25.7	467.73	54.6
13	91.78	12.51	10	100	150	15	10	120	27.2	502.11	76.8
14	92.01	13.51	10	100	150	25	10	130	0	583.82	36.6

Again, subfault parameters are required to calculate the seabed displacement, caused by the earthquake. Since there are uncertainties in the inverted parameters, different earthquake parameters have been proposed in the literature (Ammon et al., 2005; Chlieh et al., 2007; Fujii and Satake, 2007; Gopinathan et al., 2017; Hirata et al., 2006; Merrifield et al., 2005; Poisson et al., 2011; Rhie et al., 2007). Here, the parameters have been taken from (Hirata et al., 2006). Moreover, for the dynamic rupture parameters such as rise time and rupture initiation time, we use the data given by Gopinathan et al. (Gopinathan et al., 2017). To this end, the velocity rupture and rise times have been taken from Fig. 7 in (Gopinathan et al., 2017) and the rupture initiation time is calculated by (1). The fault parameters used in this paper are given in Table 1. For this tsunami, the total number of subfaults is $N_f = 14$. The length of the subfaults in the strike direction is 100 km and 150 km in the dip direction. The fault is situated between 2.13° and 13.51° northern latitude and between 91.48° and 95.54° eastern longitude. With the fault parameters given in Table 1, and using the static rupture approach, we use (2) to obtain the displacement shown in Fig. 6. As shown in this figure, the seabed displacement in subfaults 4, 6, 12 and 13 is much larger than

the displacement in other subfaults. Moreover, the figure displays points that are related to Jason-1 and TOPEX/Poseidon satellite data, which will be used to examine the numerical results. The bathymetry in the subfaults is illustrated in Fig. 6. As opposed to the Tohoku earthquake, we observe that the bathymetry at the fault is much shallower. As the wave speed is proportional to the square root of the water depth, nonlinear effects can change the tsunami behavior if the ratio of seabed displacement to bathymetry depth becomes large. In the Sumatra-Andaman case this ratio is larger but remains small enough for these nonlinearities to be negligible.

The seabed displacement as a function of time is modeled by (3) with maximum upward and downward displacements of 12 and 7 meters while the maximum water depth is about 5000m. The changes in the seabed are more complex than in the Tohoku case. Not only is the fault very long but also the rupture time is longer than for the Tohoku case. These earthquake characteristics make this problem challenging for tsunami simulation. As shown in Table 1, subfaults are activated sequentially. Thus, capturing the transient motion of the seabed displacement is likely to be important.

The mesh generated for the Sumatra-Andaman tsunami event is shown in Fig. 7. Similar to the Tohoku tsunami simulation, the initial mesh is an unrefined icosahedral mesh. The area of interest is defined by a circle of radius 40° around the point at 84° longitude and -10° latitude. The grid in this area is refined six times, resulting in a mesh with 30378 elements located in the Indian Ocean. This mesh has about twice the number of elements compared to the one used in the Tohoku tsunami simulation. There are small islands near the source, so a finer grid in comparison to the Tohoku tsunami simulation is required.
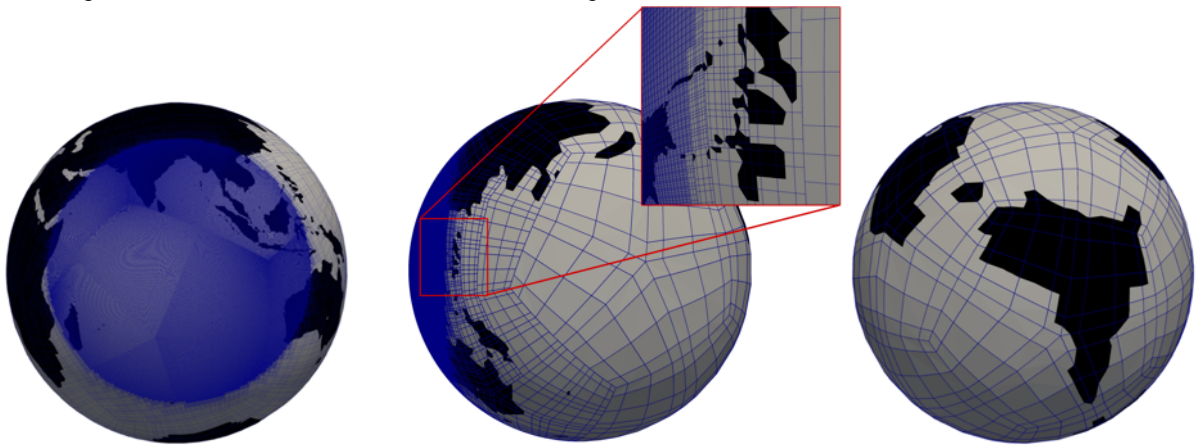

Figure 7: Front, side and back views of the mesh used for the simulation of the Sumatra-Andaman tsunami. We provide a detailed explanation of how the mesh is generated within the text.

The propagation of the tsunami waves are shown for different times in the left column of Fig. 8. In this figure, changes in water height obtained using the static rupture approach and biquartic polynomial $N = 4$ are shown. As illustrated in the figure, the seabed displacement has been translated to the water height at the initial time, since the static (instantaneous) approach is used. After a while, tsunami waves propagate into the Indian Ocean and waves become smaller.

The differences in the numerical results between the static and dynamic displacement models are shown in the middle and right columns of Fig. 8. The results presented in the right column show that the differences between the models are more prevalent in the near-field of the tsunami source. It can be seen that big waves affect a relatively small area in the vicinity of the source. If we consider the smaller differences, shown in the middle column, it is clear that the differences are significant even in the far-field. It is also evident that the dynamic model has a more substantial impact in the case of the Sumatra case. While the large differences between the two models are restricted to a relatively small region in the Tohoku case, this region is much larger for the Sumatra-Andaman tsunami. The use of the dynamic approach can therefore be advantageous even for results in the far-field. Note that for the Tohoku earthquake the major seabed displacements are mostly located on the eastern side of the fault, whereas they are located in all subfaults in the Sumatra-Andaman case. Furthermore, the rupture time of the Sumatra-Andaman earthquake is much longer than that of the Tohoku event, so that differences between the static and dynamic approaches are expected to play a bigger role in the former case.
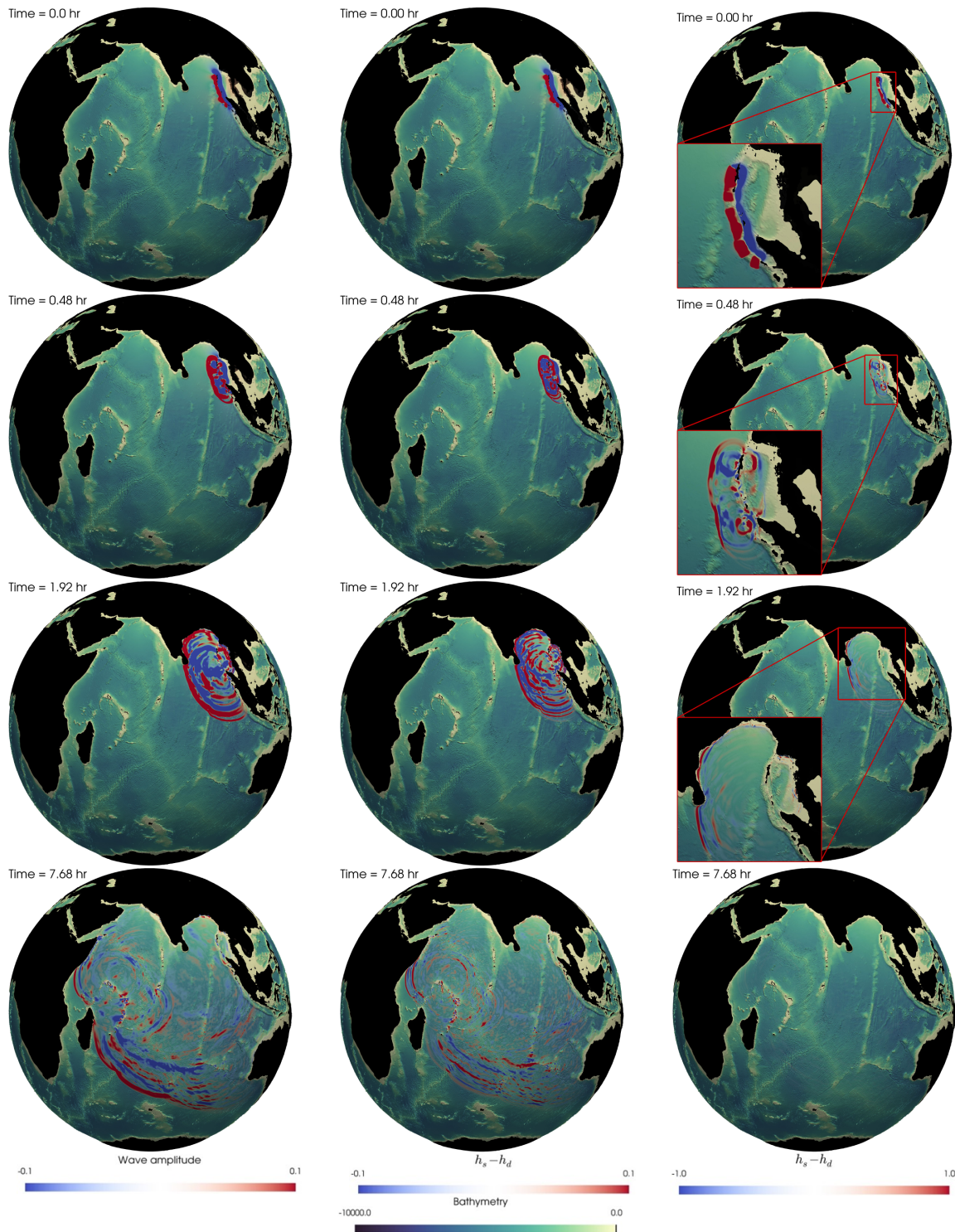
Figure 8: Propagation of tsunami waves and differences in wave amplitude between static and dynamic seabed deformations for the Sumatra-Andaman tsunami. The left column indicates the propagation of tsunami waves, the middle column highlights small differences between -0.1m and 0.1m and the right column highlights large differences between -1m and 1m.

To examine the accuracy of the numerical results computed with the static and dynamic seabed deformation models, we compare the results to satellite altimeter data. This data can be used to compute the sea surface height (SSH) along the trajectory of the satellite. Here, we use the data from two satellites namely, Jason-1 and TOPEX/Poseidon, which passed over the Indian Ocean while the tsunami occurred. Jason-1 captured SSHs about 1.9 hours after the earthquake. It passes from south to north and its altimeter measurement is numbered cycle 109 on pass 129. TOPEX/Poseidon captured the SSHs about 2.0 hours after the occurrence of the earthquake. It passes from south to north and its altimeter measurement is numbered cycle 452 on pass 129. The pass of these two

satellites and their trajectory relative to the fault is shown in Fig. 6. The altimeter data from these two satellites are available online on the Radar Altimeter Database System web site of the Department of Earth Observation and Space Systems (Scharroo et al., 2012). The measurements of the SSH from satellites does not only include the tsunami signals but also other oceanographic effects (Fujii and Satake, 2007). To obtain tsunami signals, the SSH data from previous cycles is used. Therefore, tsunami signals related to Jason-1 are obtained by subtracting measurements of cycles 109 and 108 and for TOPEX/Poseidon, it is obtained by subtracting measurements of cycles 452 and 451. Since the SSH locations in previous cycles may not be the same as those during the tsunami, a linear interpolation is used to estimate the values at the same locations. Here, it is assumed that oceanographic effects are the same in both cycles, so the difference between these two cycles gives the tsunami signals (Fujii and Satake, 2007).

To understand the effect of the polynomial degree on the numerical results, polynomial degrees of $N = 2$ and $N = 4$ are used in the simulations, and their results are compared with the measurements from Jason-1 satellite in Fig. 9. The arrival time calculated by utilizing $N = 2$ and 4 are acceptable, while wave amplitudes are better estimated by applying $N = 4$. The biquartic polynomials have lower numerical dissipation and therefore capture water wave heights in the far-field more accurately.
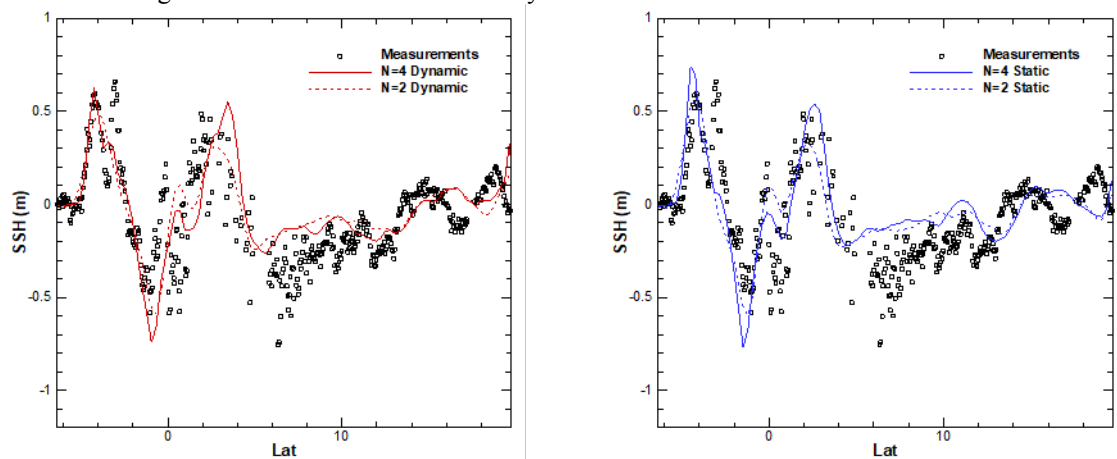

Figure 9: Effect of the polynomial degree on the computed sea surface height and comparison with Jason-1 satellite measurements. Left: Results computed with the dynamic seabed deformation approach. Right: Results computed with the static seabed deformation approach.
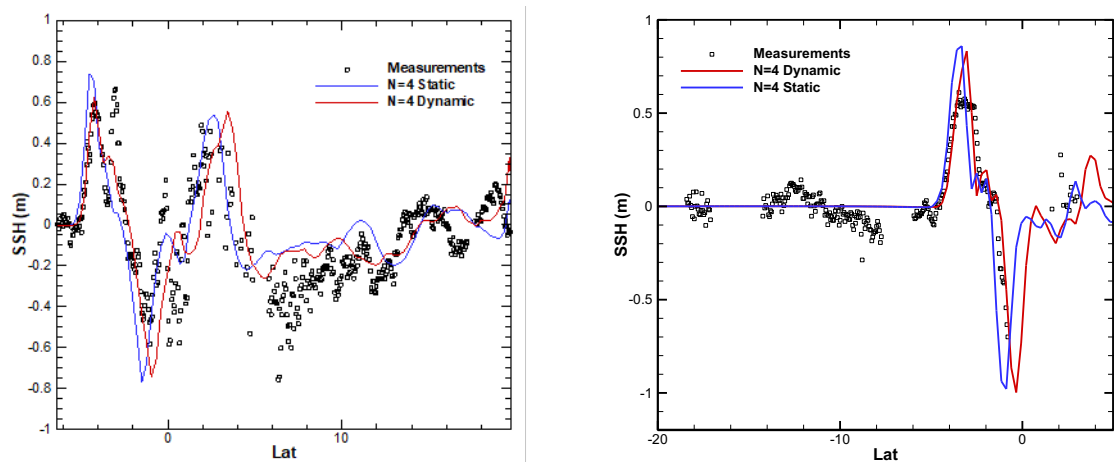

Figure 10: Effect of the seabed deformation approach on the computed sea surface height. Left: Comparison to data obtained from the Jason-1 satellite. Right: Comparison to data obtained from the TOPEX/Poseidon satellites.
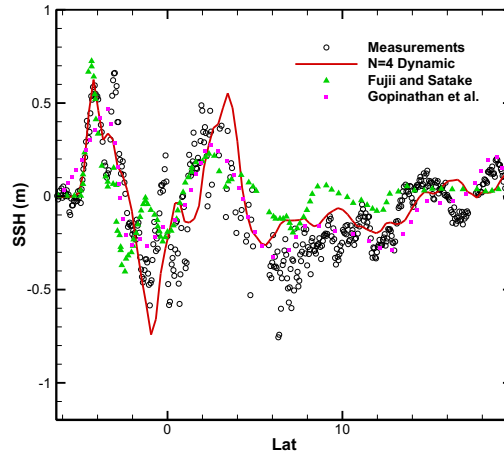
Figure 11: Comparison of computed results with numerical results presented by Fujii and Satake (Fujii and Satake, 2007) and Gopinathan et al. (Gopinathan et al., 2017).
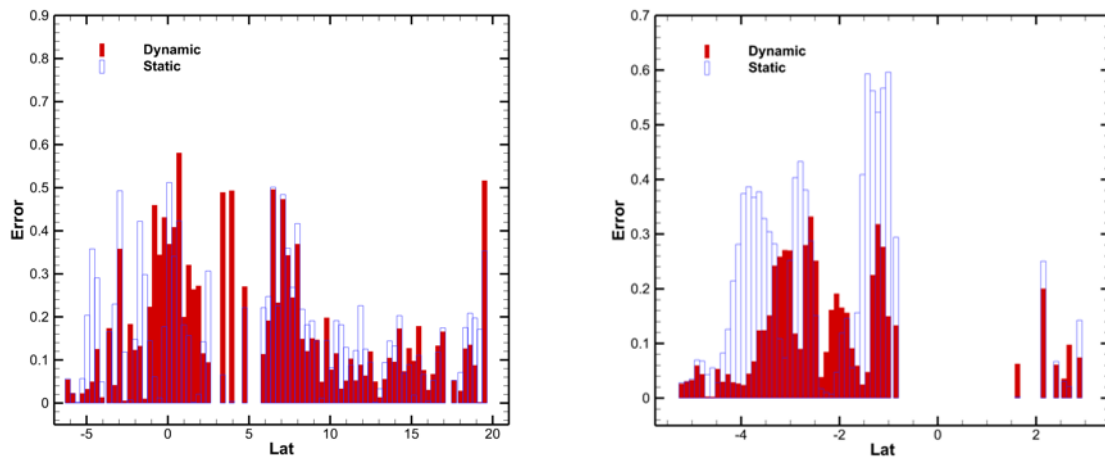

Figure 12: Effect of the seabed deformation method on the error defined by the absolute difference of the computed sea surface height and the measured sea surface height. Left: Errors based on Jason-1 data. Right: Errors based on TOPEX/Poseidon measurements.

The numerical results obtained with the static and dynamic seabed displacement models are compared to the satellite data in Fig. 10. Contrary to the Tohoku case, results obtained for the Sumatra-Andaman tsunami show that there is a substantial difference between the two models. This is clear in Fig. 10, where differences between the static and dynamic approaches are more significant at higher latitudes, whereas in lower latitudes there is a relatively small difference between the two models. The reason is that the southern subfault is activated first and the last one to be activated is the northern subfault. Therefore, for points that are mainly affected by the southern subfault, there is a small difference between both source models, while for points that are affected by the northern subfault, there is a substantial difference between the two approaches. As shown in the figure, the dynamic approach outperforms the static one, as it predicts maximum amplitudes and widths of waves with improved accuracy.

Fig. 11 shows our numerical results in comparison to results obtained by Fujii and Satake (Fujii and Satake, 2007) using a Finite Difference method for the linearized shallow water equations and numerical results obtained by Gopinathan et al. (Gopinathan et al., 2017) using a Finite Volume method. We observe good agreement of all numerical methods, especially for the arriving time and the amplitude of the first peak. In the far-field however, we observe that the proposed method captures amplitudes particularly well. While the improvement using the dynamic method seems small, we have to keep in mind that the satellite data only provides a one-dimensional extract of the wave-field to assess the accuracy of the results. Based on Fig. 8 however, we can expect that this improvement persists throughout the far-field, as we have seen that smaller differences in amplitudes remain noticeable in the far-field. Considering that wave amplitudes are smaller in the far-field, this indicates that a dynamic seabed deformation model should be considered, if a high accuracy is desired in the far-field. As indicated by Fig. 10, this is especially the case for high-order methods, which are able to capture wave amplitudes accurately in the far-field.

This is further investigated in Fig. 12, which shows errors, based on the absolute difference between the

numerical results and the satellite measurements. The errors are obtained based on two sequential cycles of the satellites. In other words, points that only exist in one cycle are not considered for evaluating the errors, as they are less reliable. From the comparison of the numerical results with Jason-1 data presented in Fig. 10, it can be concluded that within latitudes -1 to 6, the static model yields better results than the dynamic model and in the case of TOPEX/Poseidon, it can be seen that apart from latitudes -2.5 to -1.5, the dynamic model gives more accurate results than the static model. This is also reflected by the error plots in Fig. 12. Overall, we conclude that the dynamic earthquake model yields more precise and reliable results than the static model. This is reflected by the L2-norm of the resulting errors. In the TOPEX/Poseidon data, the L2-norm of the resulting errors by applying the static model is 0.2775 and 0.1527 for the dynamic model. For the Jason-1 data however, the errors for both models are 0.2047 and 0.2048 and therefore practically the same. This indicates that, the dynamical approach can provide better numerical results than the static approach, depending on the position of interest.

4. Conclusion

In this paper, a discontinuous Galerkin method was applied to model the shallow water equations on the rotating sphere with Coriolis force to simulate two large-scale tsunami events. The DG method uses curved elements and takes wetting/drying into account while also being well-balanced. We use two different approaches to model the initial seabed displacement, caused by the underwater earthquake. These are the static and dynamic displacement models. The numerical results were compared to measurements for the 2011 Tohoku and the 2004 Sumatra-Andaman tsunami events, with the goal of comparing and examining both source models and their impact on the accuracy of the numerical results. Some conclusions and remarks regarding the presented work are as follows:

Comparison of the numerical results with measurements from satellites and buoy data shows that the presented DG method by utilizing high polynomial degrees can predict key features of the tsunamis such as the arrival time and sea surface heights accurately, with satisfactory agreements between numerical results and the measurements both in the far- and near-field. Due to the good agreement with data and the high efficiency of the present method, it is a suitable candidate for tsunami early warning systems for large-scale events. This holds especially true if the far-field is of interest, where the high-order method outperformed the lower-order method in terms of accuracy.

The comparison of static and dynamic source models reveals that the impact of the dynamic approach on numerical results can be significant. In the near-field, the differences between both approaches are large, however, the choice of source did not impact the prediction of arrival times and amplitudes in a significant way, but rather the width of the first peak. On the other hand, effects of the dynamic seabed displacement play a role in the far-field, especially considering the smaller amplitudes of waves. Therefore, an important factor in choosing the seabed displacement model includes how accurate results need to be and where the zone of interest lies with respect to the tsunami source. If the zone of interest is located near the source or if accurate results are required in the far-field, a dynamic approach should be considered. Moreover, the fault length and the rupture time have a big impact on the near-field. Based on the numerical results, long faults with long rupture times require an accurate dynamical source model.

In this work, we have only considered linear activation functions for the dynamic model but an examination of other rise functions or other dynamic source models is essential to understand the effects of the earthquake modeling on the tsunami results. Moreover, there is a lot of uncertainty in the source data and the bottom topography which may affect the accuracy of the numerical results.

Acknowledgments

References

Ammon, C.J., Ji, C., Thio, H.-K., Robinson, D., Ni, S., Hjorleifsdottir, V., Kanamori, H., Lay, T., Das, S., Helmberger, D., Ichinose, G., Polet, J., Wald, D., 2005. Rupture Process of the 2004 Sumatra-Andaman Earthquake. Science 308, 1133.

Asai, M., Miyagawa, Y., Idris, N.a., Muhari, A., Imamura, F., 2016. Coupled Tsunami Simulations Based on a 2D Shallow-Water Equation-Based Finite Difference Method and 3D Incompressible Smoothed Particle

Hydrodynamics. Journal of Earthquake and Tsunami 10, 1640019.

Baba, T., Allgeyer, S., Hossen, J., Cummins, P.R., Tsushima, H., Imai, K., Yamashita, K., Kato, T., 2017. Accurate numerical simulation of the far-field tsunami caused by the 2011 Tohoku earthquake, including the effects of Boussinesq dispersion, seawater density stratification, elastic loading, and gravitational potential change. Ocean Modelling 111, 46-54.

Baba, T., Takahashi, N., Kaneda, Y., Ando, K., Matsuoka, D., Kato, T., 2015. Parallel Implementation of Dispersive Tsunami Wave Modeling with a Nesting Algorithm for the 2011 Tohoku Tsunami. Pure and Applied Geophysics 172, 3455-3472.

Blaise, S., St-Cyr, A., 2012. A dynamic hp-adaptive discontinuous Galerkin method for shallow-water flows on the sphere with application to a global tsunami simulation. Monthly Weather Review 140, 978-996.

Blaise, S., St-Cyr, A., Mavriplis, D., Lockwood, B., 2013. Discontinuous Galerkin unsteady discrete adjoint method for real-time efficient tsunami simulations. Journal of Computational Physics 232, 416-430.

Bonev, B., Hesthaven, J.S., Giraldo, F.X., Kopera, M.A., 2018. Discontinuous Galerkin scheme for the spherical shallow water equations with applications to tsunami modeling and prediction. Journal of Computational Physics 362, 425-448.

Brecht, R., Bihlo, A., MacLachlan, S., Behrens, J., 2018. A well-balanced meshless tsunami propagation and inundation model. Advances in Water Resources 115, 273-285.

Castro, C.E., Behrens, J., Pelties, C., 2016. Optimization of the ADER-DG method in GPU applied to linear hyperbolic PDEs. International Journal for Numerical Methods in Fluids 81, 195-219.

Chlieh, M., Avouac, J.-P., Hjorleifsdottir, V., Song, T.-R.A., Ji, C., Sieh, K., Sladen, A., Hebert, H., Prawirodirdjo, L., Bock, Y., 2007. Coseismic slip and afterslip of the great M w 9.15 Sumatra–Andaman earthquake of 2004. Bulletin of the Seismological Society of America 97, S152-S173.

Clain, S., Reis, C., Costa, R., Figueiredo, J., Baptista, M.A., Miranda, J.M., 2016. Second-order finite volume with hydrostatic reconstruction for tsunami simulation. Journal of Advances in Modeling Earth Systems 8, 1691-1713.

de la Asunción, M., Castro, M.J., Mantas, J.M., Ortega, S., 2016. Numerical simulation of tsunamis generated by landslides on multiple GPUs. Advances in Engineering Software 99, 59-72.

Dutykh, D., Dias, F., 2009. Tsunami generation by dynamic displacement of sea bed due to dip-slip faulting. Mathematics and Computers in Simulation 80, 837-848.

Dutykh, D., Mitsotakis, D., Gardeil, X., Dias, F., 2013. On the use of the finite fault solution for tsunami generation problems. Theoretical and Computational Fluid Dynamics 27, 177-199.

Ezzedine, S.M., Lomov, I., Miller, P.L., Dennison, D.S., Dearborn, D.S., Antoun, T.H., 2015. Simulation of asteroid impact on ocean surfaces, subsequent wave generation and the effect on US shorelines. Procedia Engineering 103, 113-120.

Flouri, E.T., Kalligeris, N., Alexandrakis, G., Kampanis, N.A., Synolakis, C.E., 2013. Application of a finite difference computational model to the simulation of earthquake generated tsunamis. Applied Numerical Mathematics 67, 111-125.

Fujii, Y., Satake, K., 2007. Tsunami source of the 2004 Sumatra–Andaman earthquake inferred from tide gauge and satellite data. Bulletin of the Seismological Society of America 97, S192-S207.

Giraldo, F.X., Hesthaven, J.S., Warburton, T., 2002. Nodal High-Order Discontinuous Galerkin Methods for the Spherical Shallow Water Equations. Journal of Computational Physics 181, 499-525.

Gopinathan, D., Venugopal, M., Roy, D., Rajendran, K., Guillas, S., Dias, F., 2017. Uncertainties in the 2004 Sumatra–Andaman source through nonlinear stochastic inversion of tsunami waves. Proceedings of the Royal Society A: Mathematical, Physical and Engineering Sciences 473, 20170353.

Gottlieb, S., Ketcheson, D., Shu, C.-W., 2011. Strong Stability Preserving Runge-Kutta and Multistep Time Discretizations. WORLD SCIENTIFIC.

Hirata, K., Satake, K., Tanioka, Y., Kuragano, T., Hasegawa, Y., Hayashi, Y., Hamada, N., 2006. The 2004 Indian Ocean tsunami: Tsunami source model from satellite altimetry. Earth, Planets and Space 58, 195-201.

Kundu, A., 2007. Tsunami and nonlinear waves. Springer.

LeVeque, R.J., George, D.L., Berger, M.J., 2011. Tsunami modelling with adaptively refined finite volume methods. Acta Numerica 20, 211-289.

Merrifield, M.A., Firing, Y.L., Aarup, T., Agricole, W., Brundrit, G., Chang-Seng, D., Farre, R., Kilonsky, B., Knight, W., Kong, L., Magori, C., Manurung, P., McCreery, C., Mitchell, W., Pillay, S., Schindele, F., Shillington, F., Testut, L., Wijeratne, E.M.S., Caldwell, P., Jardin, J., Nakahara, S., Porter, F.Y., Turetsky, N., 2005. Tide gauge observations of the Indian Ocean tsunami, December 26, 2004. Geophysical Research Letters 32.

Milburn, H.B., Nakamura, A.I., Gonzalez, F.I., 1996. Deep-ocean Assessment and Reporting of Tsunamis (DART): Real-Time Tsunami Reporting from the Deep Ocean. NOAA Online Report.

Mori, N., Yoneyama, N., Pringle, W., 2015. Effects of the Offshore Barrier Against the 2011 Off the Pacific Coast of Tohoku Earthquake Tsunami and Lessons Learned, Post-Tsunami Hazard: Reconstruction and Restoration. Springer International Publishing, Cham, pp. 121-132.

Ohmachi, T., Tsukiyama, H., Matsumoto, H., 2001. Simulation of Tsunami Induced by Dynamic Displacement of Seabed due to Seismic Faulting. Bulletin of the Seismological Society of America 91, 1898-1909.

Ohta, Y., Kobayashi, T., Tsushima, H., Miura, S., Hino, R., Takasu, T., Fujimoto, H., Iinuma, T., Tachibana, K., Demachi, T., Sato, T., Ohzono, M., Umino, N., 2012. Quasi real-time fault model estimation for near-field tsunami forecasting based on RTK-GPS analysis: Application to the 2011 Tohoku-Oki earthquake (Mw 9.0). Journal of Geophysical Research: Solid Earth 117.

Oishi, Y., Piggott, M.D., Maeda, T., Kramer, S.C., Collins, G.S., Tsushima, H., Furumura, T., 2013. Three-dimensional tsunami propagation simulations using an unstructured mesh finite element model. Journal of Geophysical Research: Solid Earth 118, 2998-3018.

Okada, Y., 1985. Surface deformation due to shear and tensile faults in a half-space. Bulletin of the seismological society of America 75, 1135-1154.

Olabarrieta, M., Medina, R., Gonzalez, M., Otero, L., 2011. C3: A finite volume-finite difference hybrid model for tsunami propagation and runup. Computers & Geosciences 37, 1003-1014.

Ortega, E., Oñate, E., Idelsohn, S., Buachart, C., 2011. An adaptive finite point method for the shallow water equations. International Journal for Numerical Methods in Engineering 88, 180-204.

Poisson, B., Oliveros, C., Pedreros, R., 2011. Is there a best source model of the Sumatra 2004 earthquake for simulating the consecutive tsunami? Geophysical Journal International 185, 1365-1378.

Rannabauer, L., Dumbser, M., Bader, M., 2018. ADER-DG with a-posteriori finite-volume limiting to simulate tsunamis in a parallel adaptive mesh refinement framework. Computers & Fluids 173, 299-306.

Reckinger, S.M., Vasilyev, O.V., Fox-Kemper, B., 2014. Adaptive wavelet collocation method on the shallow water model. Journal of Computational Physics 271, 342-359.

Rhie, J., Dreger, D., Bürgmann, R., Romanowicz, B., 2007. Slip of the 2004 Sumatra–Andaman earthquake from joint inversion of long-period global seismic waveforms and GPS static offsets. Bulletin of the Seismological Society of America 97, S115-S127.

Saito, T., Furumura, T., 2009. Three-dimensional simulation of tsunami generation and propagation: Application to intraplate events. Journal of Geophysical Research: Solid Earth 114.

Scharroo, R., Leuliette, E.W., Lillibridge, J.L., Byrne, D., Naeije, M.C., Mitchum, G.T., 2012. RADS: Consistent multi-mission products, Symposium on 20 Years of Progress in Radar Altimetry,.

Seny, B., Lambrechts, J., Toulorge, T., Legat, V., Remacle, J.-F., 2014. An efficient parallel implementation of explicit multirate Runge–Kutta schemes for discontinuous Galerkin computations. Journal of Computational Physics 256, 135-160.

Shao, G., Li, X., Ji, C., Maeda, T., 2011. Focal mechanism and slip history of the 2011 M w 9.1 off the Pacific coast of Tohoku Earthquake, constrained with teleseismic body and surface waves. Earth, planets and space 63, 9.

Suppasri, A., Imamura, F., Koshimura, S., 2010. Effects of the Rupture Velocity of Fault Motion, Ocean Current and Initial Sea Level on the Transoceanic Propagation of Tsunami. Coastal Engineering Journal 52, 107-132.

Takase, S., Moriguchi, S., Terada, K., Kato, J., Kyoya, T., Kashiyama, K., Kotani, T., 2016. 2D–3D hybrid stabilized finite element method for tsunami runup simulations. Computational Mechanics 58, 411-422.

Ulvrova, M., Paris, R., Nomikou, P., Kelfoun, K., Leibrandt, S., Tappin, D.R., McCoy, F.W., 2016. Source of the tsunami generated by the 1650AD eruption of Kolumbo submarine volcano (Aegean Sea, Greece). Journal of Volcanology and Geothermal Research 321, 125-139.

Uphoff, C., Rettenberger, S., Bader, M., Madden, E.H., Ulrich, T., Wollherr, S., Gabriel, A.-A., 2007. Extreme scale multi-physics simulations of the tsunamigenic 2004 sumatra megathrust earthquake, Proceedings of the International Conference for High Performance Computing, Networking, Storage and Analysis, pp. 1-16.

Vogl, C.J., LeVeque, R.J., 2017. A High-Resolution Finite Volume Seismic Model to Generate Seafloor Deformation for Tsunami Modeling. Journal of Scientific Computing 73, 1204-1215.

Wang, X., Liu, P.L.F., 2007. Numerical simulations of the 2004 Indian ocean tsunamis - coastal effects. Journal of Earthquake and Tsunami 01, 273-297.

Xing, Y., Zhang, X., Shu, C.-W., 2010. Positivity-preserving high order well-balanced discontinuous Galerkin methods for the shallow water equations. Advances in Water Resources 33, 1476-1493.

Yamazaki, Y., Cheung, K.F., Kowalik, Z., 2011a. Depth-integrated, non-hydrostatic model with grid nesting for tsunami generation, propagation, and run-up. International Journal for Numerical Methods in Fluids 67, 2081-2107.

Yamazaki, Y., Lay, T., Cheung, K.F., Yue, H., Kanamori, H., 2011b. Modeling near-field tsunami observations to improve finite-fault slip models for the 11 March 2011 Tohoku earthquake. Geophysical Research Letters 38.

Appendix A. Governing equations

We consider the spherical shallow water equations as presented in (Giraldo et al., 2002). The depth-averaged equations are solved in a Cartesian frame related to the earth to avoid numerical problems associated with the

spherical formulation of the problem. This comes at the cost of an additional equation as the velocity vector $p = \{u, v, w\}^T$ contains three components. Tangentiality of the velocity vector to the surface of the Earth is enforced through a Lagrange multiplier. The system of conservation laws can be written as

$$\frac{\partial q}{\partial t} + \nabla . F = S \tag{A1}$$

where q, $F = f_x \hat{\imath} + f_y \hat{\jmath} + f_z \hat{k}$ and S are the solution, the flux and the source vectors, respectively. These are given as

$$q = \begin{bmatrix} \varphi \\ \varphi u \\ \varphi v \\ \varphi w \end{bmatrix}, \qquad f_x = \begin{bmatrix} \varphi u \\ \varphi u^2 + \dfrac{\varphi^2}{2} \\ \varphi uv \\ \varphi uw \end{bmatrix}, \qquad f_y = \begin{bmatrix} \varphi v \\ \varphi uv \\ \varphi v^2 + \dfrac{\varphi^2}{2} \\ \varphi vw \end{bmatrix}, \qquad f_z = \begin{bmatrix} \varphi w \\ \varphi uw \\ \varphi uw \\ \varphi w^2 + \dfrac{\varphi^2}{2} \end{bmatrix}, \qquad S = \begin{bmatrix} 0 \\ \tilde{S} \end{bmatrix} \tag{A2}$$

where $\hat{\imath}$, $\hat{\jmath}$ and $\hat{k}$ are the unit vectors in the Cartesian coordinates $r = \{x, y, z\}^T$. Here, $\varphi = gh$ denotes the geopotential height, where g and h are the gravitational acceleration and the water column height, respectively. The source term acts only on the momentum equations, and consists of

$$\tilde{S} = -\frac{2\omega z \varphi}{R^2} r \times p - \varphi \nabla \tau + \mu r. \tag{A3}$$

The first term in (A3) is the Coriolis force, the second one is the pressure gradient due to the bathymetry and the last term forces the velocity vector to be tangential to the spherical shell, i.e., $p . r = 0$. The angular velocity of the sphere ω is defined based on the rotation around the z-axis, where R is the radius of the earth. The bottom topography $\tau = gb$ is measured in geopotential units where b is the bathymetry relative to the sea level. The Lagrange multiplier μ is defined as

$$\mu = \frac{1}{R^2} r . \left(\varphi \nabla \tau + \nabla . \tilde{F} \right) \tag{A4}$$

where $\tilde{F}$ is the part of the flux that acts on the momentum equations.

Appendix B. Numerical method

The governing equations in the previous section are solved using the numerical method discussed in detail in (Bonev et al., 2018). We give a short overview of the method and refer the reader for details to (Bonev et al., 2018). The computational domain Ω with boundary $\partial\Omega$, is divided into K non-overlapping elements. As Ω is the two-dimensional sphere with radius R, elements are curved quadrilaterals of arbitrary sizes and we denote them as D^k. Thus, Ω is the union of D^k, i.e.,

$$\Omega = \bigcup_{k=1}^{K} D^k. \tag{A5}$$

To make the computations easier, the mapping $\xi = \psi(x)$ is used to transform coordinates from the physical space $r = \{x, y, z\}^T$ to the reference domain $\rho = \{\xi, \eta\}^T$. The numerical solution q_N is expressed as piecewise polynomials

$$q \approx q_N = \bigoplus_{k=1}^{K} q_N^k \tag{A6}$$

where q_N^k can be expressed as a linear combination

$$q_N^k(r, t) = \sum_{m=1}^{(N+1)^2} q_N^k\left(r(\rho_m), t\right) L_m(\rho(r)) \tag{A7}$$

of the basis functions L_m which are formed using the tensor-product

$$L_m(\rho) = l_i(\xi) l_j(\eta) \tag{A8}$$

of the one-dimensional Lagrange polynomials

$$l_i(\xi) = \prod_{\substack{j=1 \\ j \neq i}}^{N+1} \frac{\xi - \xi_j}{\xi_i - \xi_j} \tag{A9}$$

of polynomial degree N. These polynomials have the nodal property $l_i\left(\xi_j\right) = \delta_{ij}$ where δ_{ij} is the Kronecker delta. The nodes ξ_j are chosen to be the Legendre-Gauss-Lobatto (LGL) nodes, which are defined on the interval $[-1, 1]$. As a consequence, the reference element in computational space is $I = [-1, 1]^2$. Applying the weighted residual method to the governing equations (A1), yields

$$\int_D \left(\frac{\partial \boldsymbol{q}}{\partial t} + \nabla . \, \boldsymbol{F} - \boldsymbol{S} \right) \phi(\boldsymbol{r}) \, d\boldsymbol{r} = \int_I \left(\frac{\partial \boldsymbol{q}}{\partial t} + \nabla . \, \boldsymbol{F} - \boldsymbol{S} \right) \phi(\boldsymbol{\rho}) \, J_D \, d\boldsymbol{\rho} = 0 \tag{A10}$$

where ϕ is a test function. To derive the nodal version of the discontinuous Galerkin method, the test and shape functions are set equal to each other, thus $\phi_m = L_m$. The strong form of the nodal discontinuous Galerkin method is recovered as

$$\int_I \left(\frac{\partial \boldsymbol{q}_N}{\partial t} + \nabla . \, \boldsymbol{F}_N - \boldsymbol{S}_N \right) L_i J_D d\boldsymbol{\rho} = - \oint_{\partial I} \hat{\boldsymbol{n}} . \left(\boldsymbol{F}_N - \boldsymbol{F}_N^* \right) L_i J_{\partial D} d\boldsymbol{\rho} \tag{A11}$$

where $\hat{n}$, J_D and $J_{\partial D}$ are the outward unit normal to the edge of element, the Jacobian of the element and the Jacobian of the edge parametrization, respectively. Due to the discontinuous nature of the solution, a suitable numerical flux $\boldsymbol{F}^*$ must be defined to connect the solution across interfaces. We use the local Lax-Friedrichs numerical flux

$$\boldsymbol{F}_N^* = \frac{1}{2} \left(\boldsymbol{F}_N^* \left(\boldsymbol{q}_N^- \right) + \boldsymbol{F}_N^* \left(\boldsymbol{q}_N^+ \right) \right) - \frac{c}{2} \left(\boldsymbol{q}_N^+ - \boldsymbol{q}_N^- \right) \tag{A12}$$

where the superscripts – and + refer to values within the element and neighboring element, respectively. The factor c is the maximum local wave speed across the element boundary, given as

$$c = \max \left\{ \left| \hat{\boldsymbol{n}} . \, \boldsymbol{p}_N^- \right| + \sqrt{\varphi_N^-} \, , \quad \left| \hat{\boldsymbol{n}} . \, \boldsymbol{p}_N^+ \right| + \sqrt{\varphi_N^+} \right\}. \tag{A13}$$

The spatial discretization can be extended to nonconforming meshes as discussed in (Bonev et al., 2018). In this study, $N = 2$ and 4 are utilized for simulating tsunamis in order to investigate the effect of polynomial degree on the numerical results. Although it is feasible to use the higher-order methods by considering higher Ns, the fifth-order methods ($N = 4$) are commonly used for simulating fluid flows in the literature and they provide very accurate numerical results with a reasonable computational cost. Note that, a higher polynomial degree can be used if a coarse grid used in the area of interest which is not the case here.

Finally, to complete the numerical scheme, the integrals in (A11) have to be computed numerically. To this end, quadrature rules for the approximation of the volume and the surface integral terms are used. Thus, we obtain a system of ordinary differential equations in the form of

$$\frac{\partial \boldsymbol{q}_N}{\partial t} = \boldsymbol{R}_N(\boldsymbol{q}_N), \tag{A14}$$

where $\boldsymbol{R}_N$ is the right-hand side obtained by applying the quadrature rules in the discontinuous Galerkin formulation. Here, a three-step, third-order strong stability preserving Runge-Kutta method is used to solve this semi-discrete form (Gottlieb et al., 2011).

Appendix C. Wet/Dry treatment

The task of performing tsunami simulations using the shallow water model requires the use of an inundation model. This inundation model handels the change in shape and topology of the domain as well as the numerical challenges that arise in drying domains.

To take care of inundation, we follow the method described in (Bonev et al., 2018). We call a node $\boldsymbol{x}_i$ dry if the water height $\varphi_N(\boldsymbol{x}_i)$ is smaller than a certain tolerance φ_{tol} and distinguish between wet, dry and semi-dry elements. The latter contains both wet and dry nodes, which pose difficulties in the numerical treatment. More specially, such difficulties are the appearance of negative water heights, artificial pressure gradients and instabilities due to the discontinuity in the derivative of the state variables. To guarantee the positivity of the water column height, we use the method presented in (Xing et al., 2010). By controlling the timestep Δt such that

$$\frac{J_{\partial D}}{J_D} c \Delta t \leq \frac{\omega_1}{2} \tag{A15}$$

is satisfied in each cell, we guarantee positivity of the average water height φ_N^{avg} within each cell. Here $J_D, J_{\partial D}$ denote the Jacobians of the element and the edge parametrization respectively. ω_1 denotes the first quadrature weight and c denotes the maximum wave speed across the cell interface. While this will guarantee positivity of the cell averages, it will not guarantee positivity on each node. For this purpose, we apply a linear scaling if a negative water height occurs within a cell. Using the scaling factor

$$\theta = \min \left\{ 1, \frac{\varphi_N^{\text{avg}}}{\varphi_N^{\text{avg}} - \varphi_N^{\text{min}}} \right\}, \tag{A16}$$

the solution is rescaled around the cell-average of the solution. Thus, the minimum water height is set to 0, while conserving the mass within the cell.

Although these measures suffice to guarantee positivity, they are not sufficient to guarantee the well-balanced

property of the scheme. This is due to artificial pressure gradients, which occur in the evaluation of the term $\varphi_N \nabla(\varphi_N + \tau_N)$ if an element contains both wet and dry nodes. Therefore, in these elements, we replace the regular differential operator $\partial/\partial\xi$ with the finite-difference operator

$$
\mathcal{D}_\xi = \begin{cases}
\dfrac{f(\xi_{i+1}) - f(\xi_{i-1})}{\xi_{i+1} - \xi_{i-1}} & \text{if } \xi_i, \xi_{i-1}, \xi_{i+1} \text{ are wet} \\[2ex]
\dfrac{f(\xi_{i+1}) - f(\xi_i)}{\xi_{i+1} - \xi_i} & \text{if } \xi_{i+1}, \xi_i \text{ are wet and } \xi_{i-1} \text{ is dry or } i - 1 < 1 \\[2ex]
\dfrac{f(\xi_i) - f(\xi_{i-1})}{\xi_i - \xi_{i-1}} & \text{if } \xi_i, \xi_{i-1} \text{ are wet and } \xi_{i+1} \text{ is dry or } i + 1 > N \\[2ex]
0 & \text{otherwise}
\end{cases} \qquad (A17)
$$

This operator mitigates the problem of artificial pressure gradients as it switches to a local evaluation of the gradient, which ignores dry areas within the element. Finally, a filter is used to guarantee the stability of the scheme. We refer the reader to (Bonev et al., 2018) for a more detailed discussion of the inundation model.